Journal of Materials Chemistry C

ROYAL SOCIETY OF CHEMISTRY

PAPER

View Article Online
View Journal

Cite this: DOI: 10.1039/d5tc02968f

Promising magnetocaloric performance of nanostructured GdFeSi intermetallic ribbons for efficient natural gas liquefaction purposes

A. Sanz-Prada,[a] P. Alvarez-Alonso,[ab] J. L. Sánchez Llamazares,[c] L. G. Escobedo-Valadez,[c] J. S. Garitaonandia,[de] Pedro Gorria,*[ab] Jesús A. Blanco[a] and J. López-García[ab]

Received 5th August 2025,
Accepted 17th November 2025

DOI: 10.1039/d5tc02968f

rsc.li/materials-c

Some members of the RFeSi (R = Pr, Tb, Dy, Gd) family of intermetallic compounds, with tetragonal CeFeSi-type crystalline structure, exhibit low-temperature ferromagnetic behaviour. These alloys are of particular interest for two main reasons: (i) the Fe atoms appear to carry negligible or no magnetic moment, with R being solely responsible for the spontaneous magnetization; and (ii) they display a noticeable magnetocaloric effect (MCE) below 150 K. We have successfully fabricated single-phase GdFeSi ribbons in a one-step melt-spinning process, avoiding conventional thermal treatments such as long-time (several weeks) high-temperature annealing (above 1000 °C), thereby considerably reducing production costs. The ribbons show a broad entropy change leading to a relative cooling power of 517 J kg^{-1} (~3.76 J cm^{-3}) over 110–180 K, providing a useful working range despite a modest isothermal magnetic entropy peak value. Materials operating efficiently in this temperature window are relatively scarce compared with other intermetallic magnetocalorics. The magnetocaloric properties of GdFeSi ribbons, as shown by these results, make them promising for magnetic refrigeration technologies, including liquefaction processes for light hydrocarbons and industrial gases.

Introduction

Nowadays, optimizing energy consumption and ensuring environmental responsibility are two major global challenges for our society. To achieve these two objectives, solid-state refrigeration based on the magnetocaloric effect (MCE) could reduce the undesirable impacts of conventional refrigeration, which mainly arise from the production of greenhouse gases and damage to the ozone layer.[1,2] Over the last two decades, research on magnetocaloric materials has focused mainly on applications near room temperature.[3–5] However, the pursuit of new magnetocaloric materials operating below 200 K has intensified, driven by a shift towards low-temperature applications such as gas liquefaction and a scarcity of efficient materials in this range.[2,6] At these temperatures, rare-earth elements (R), their solid solutions $(R_{1-x}R'_x)$, and some R-based intermetallic compounds exhibit outstanding magnetocaloric properties.[7,8] This behaviour is attributed to the high magnetic moments of R, which contribute to a significant saturation magnetization (M_s) together with a moderate specific heat capacity. The interplay of these factors leads to excellent values for the maximum magnetic entropy ($|\Delta S_M|^{max}$) and adiabatic temperature changes ($|\Delta T_{ad}|^{max}$).[9] Some notable examples of outstanding magnetocaloric materials operating at cryogenic temperatures include intermetallic compounds based on R elements, such as $Gd_3Ga_5O_{12}$ or R–TM_2 (TM = transition metal) Laves phases.[2,6,9,10] The main technological objective in this field is the design and optimization of efficient liquefaction systems for specific gases, including natural gas components like methane (liquefaction temperature: 111.7 K), nitrogen (77 K), hydrogen (20 K), and helium (4.2 K).[8,11,12]

Several RFeSi alloys (from R = Nd to Er) exhibit low-temperature ferromagnetic order, with Curie temperature values $T_C < 150$ K.[13–19] This makes them strong candidates for achieving the aforementioned liquefaction purposes.[9,13,14] These compounds crystallize in the tetragonal CeFeSi-type crystal structure (space group *P*4/*nmm*), where R and Si atoms are located at 2a and Fe atoms at 2c Wyckoff positions.[15,16] Furthermore, density-of-states

[a] Departamento de Física, Universidad de Oviedo, Calvo Sotelo 18, 33007 Oviedo, Spain. E-mail: pgorria@uniovi.es
[b] Instituto Universitario de Tecnología Industrial de Asturias, Universidad de Oviedo, Gijón 33203, Spain
[c] Instituto Potosino de Investigación Científica y Tecnológica A.C., Camino a la Presa San José 2055, 78216, San Luis Potosí, México
[d] Faculty of Science and Technology, Universidad del País Vasco/Euskal Herriko Unibertsitatea, Barrio Sarriena s/n, Leioa 48940, Spain
[e] BCMaterials (Basque Center for Materials, Applications & Nanostructures), UPV/EHU Scientific Park, Bldg. Martina Casiano, Barrio Sarriena s/n, Leioa 48940, Spain

(DOS) calculations suggest that Fe and Si atoms do not carry any magnetic moment due to the hybridization between the Fe d-states and the Si p-states.[20] This theoretical result is corroborated by neutron diffraction studies, which confirm that only R atoms contribute to the magnetic moment.[16] However, a small value for the Fe magnetic moment has been reported in nanostructured alloys,[21] which may be induced by the magnetically ordered R sublattice.[22]

Conventional methods for fabricating these alloys as polycrystalline bulk pieces typically involve induction or arc melting, followed by high-temperature and long-duration annealing to ensure the homogeneity of the tetragonal phase (1173 K for two weeks or 1375 K for 35 days).[13,16,19,23] However, we have demonstrated that melt-spinning enables the one-step fabrication of single-phase R-based alloys, eliminating the need for further high-temperature and time-consuming treatments. Our group has developed expertise in this technique through the study of rapidly solidified R-based ribbons exhibiting significant magnetocaloric effects, such as RNi_2 (R = Tb, Dy, Ho)[24–26] or R_2Fe_{17} (R = Y, Nd, Pr).[27–29] Some of these ribbon compounds exhibit $|\Delta S_M|^{max}$ values that surpass those of their conventionally processed bulk counterparts.

In this work, we report the comprehensive analysis of the crystalline structure, microstructure, magnetic properties and magnetocaloric performance of a GdFeSi intermetallic compound synthesized *via* the melt-spinning technique. The specific objectives are to establish a structure–property relationship by correlating the structural and microstructural characteristics with the magnetic and magnetocaloric response, and to evaluate the application potential of the compound through a comparative analysis with existing materials.

Experimental methods

The ternary GdFeSi alloy was synthesized from high-purity elements (≥99.9%) by arc melting under a protective argon atmosphere. To ensure homogeneity, the ingot was remelted four times. Subsequently, melt-spun ribbons were produced using an Edmund Bühler model SC melt-spinner system at a linear wheel speed of 20 m s^{-1} under an ultra-high-purity helium atmosphere. Some of the ribbons were then powdered using an agate mortar.

High-resolution X-ray diffraction (XRD) patterns were collected at room temperature using graphite-monochromated Mo-K_α radiation (λ = 0.709 Å) on a Seifert XRD3000 diffractometer. Scans were performed over the 2θ range between 7° and 55°, with $\Delta\theta$ = 0.02° steps and counting times of 20 s per point. A LaB_6 standard was used for calibration. The Rietveld refinement of the diffraction patterns was carried out using FullProf Suite software.[30] A Thompson–Cox–Hastings pseudo-Voigt (TCHPV) function was employed to model the profiles of the Bragg diffraction peaks. Microstructural analysis was performed using the parameters obtained from the Rietveld refinement. The fitting procedure, carried out with the TCHPV function, enabled the evaluation of both crystallite size and microstrain through a generalized Scherrer peak broadening approach. The microstructural parameters were determined for each Bragg reflection, and average values were subsequently calculated.[31] The morphology and composition of the ribbons were determined through scanning electron microscopy (SEM) and dispersive X-ray microanalyses (EDX) in a model FEI ESEM-Quanta FEG-250 microscope. Magnetization measurements were carried out in a Quantum Design PPMS-9T Dynacool system using the vibrating sample magnetometer (VSM) option. The temperature dependence of the magnetization, $M(T)$ curves, was measured between 2 and 200 K at controlled heating/cooling rates of 1 K min^{-1} following zero-field-cooling (ZFC) and field-cooling (FC) protocols, and under applied magnetic field values of 5 mT and 5 T. In addition, a set of isothermal magnetization curves, $M(H)$, up to an applied magnetic field of 5 T, was measured in the temperature range from 90 to 190 K with ΔT = 1.5 K. ^{57}Fe Mössbauer spectra were collected at T = 55 and 300 K in a constant acceleration spectrometer in transmission geometry using a Co(Rh) source. Isomer shift values were taken with respect to an α-Fe calibration foil measured at room temperature.

Results and discussion

Crystalline structure and microstructural characterization

Fig. 1 shows the room temperature XRD patterns of the as-cast and powdered ribbons, along with the corresponding fits. The observed peak intensities can be indexed as Bragg diffraction reflections belonging to a CeFeSi-type tetragonal crystal structure with space group *P*4/*nmm*. The refined lattice parameters are a = 3.998(2) Å and c = 6.891(6) Å, in good agreement with previously reported values.[15,16] Small amounts of impurity phases, $GdFe_2Si_2$ (<5%) and Gd_2O_3 (≈1%), are also detected (see Fig. 1). The Rietveld refinement of the diffraction patterns confirms that Fe atoms occupy the 2*a* Wyckoff positions (0.75, 0.25, 0), while Gd and Si atoms occupy the 2c positions (0.25, 0.25, z) with Z_{Gd} = 0.67 and Z_{Si} = 0.22.

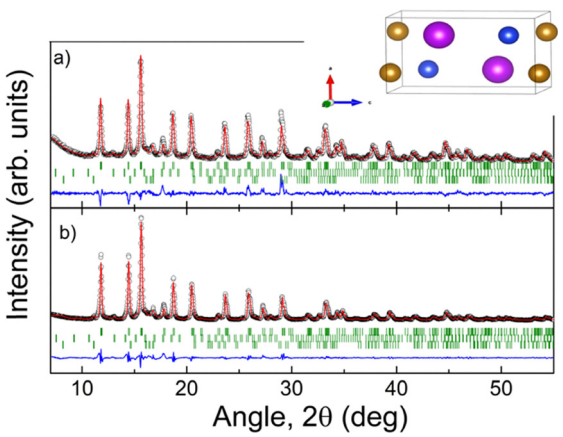

Fig. 1 Room-temperature XRD patterns for (a) ribbons, and for (b) powdered ribbons together with their fits. Black dots represent the experimental data, red and blue lines show the calculated patterns and the difference between the experimental data and calculated patterns, respectively. Vertical marks correspond to the Bragg reflections of the GdFeSi, $GdFe_2Si_2$ and Gd_2O_3 phases, respectively.

Moreover, a preferred orientation (texture) along the [110] direction is needed to properly account for the relative intensities of the Bragg peaks. This indicates that the (110) planes of the crystallites are predominantly aligned parallel to the ribbon thickness, meaning the *c*-axis tends to lie parallel to the ribbon surfaces. It is also noteworthy that the diffraction peaks are significantly broader than those expected for a polycrystalline sample with micrometer-sized grains. The peak-profile analysis gives a mean crystallite size of $\langle\tau\rangle = 25(3)$ nm where the number in parentheses indicates the standard deviation, and an induced internal microstrain of $\varepsilon = 0.15(5)\%$.

Fig. 1 also reveals a small broad bump at low angles ($2\theta < 10^{\circ}$), which is more pronounced in the as-cast sample (Fig. 1a). This feature suggests the presence of disordered or amorphous regions, likely associated with the small crystallite size and the resulting high density of the grain boundaries. These regions can accommodate vacancies generated during the synthesis process, leading to a lack of long-range crystalline order. A similar microstructure has already been reported for R_2Fe_{17} melt-spun ribbons.[27,29]

An SEM image of a GdFeSi ribbon cross-section is shown in Fig. 2. A clear difference in microstructure is observed between the two ribbon surfaces: the surface in contact with the wheel during rapid solidification (CS), and the non-contact surface (NCS). The CS side shows an accumulation of sub-micrometric grains, a feature that is not observed on the NCS side. In contrast, the NCS surface tends to form a columnar-like microstructure, which may be responsible for the previously mentioned preferential crystallographic orientation (texture). This texture likely results from the rapid solidification process, which occurs at an estimated cooling rate of $\sim 10^6$ K s^{-1}. EDX analysis confirms that the relative concentrations of Gd, Fe, and Si are close to the nominal 1 : 1 : 1 composition.

Specifically, the crystallite size ($\sim$25 nm) obtained from XRD is smaller than the grain size ($\sim$1–2 μm) seen in SEM, as expected. This difference arises because each SEM-observed grain can comprise multiple coherently scattering domains (crystallites) separated by low-angle boundaries or sub-grain structures. The comparison highlights the polycrystalline nature of the ribbons and provides a more complete understanding of the microstructure.

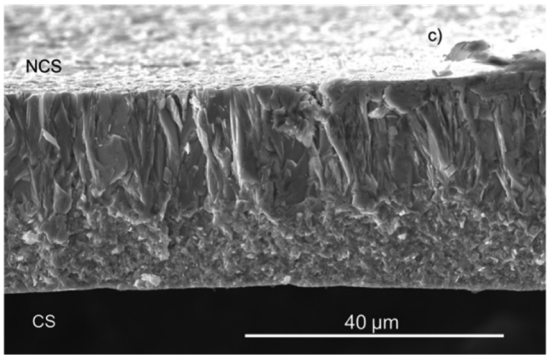

Fig. 2 Cross-sectional SEM micrograph of the GdFeSi ribbon. CS and NCS indicate the contact (wheel) and non-contact (air) surfaces, respectively.

Magnetic behaviour

The temperature dependence of the magnetization, $M(T)$, confirms the existence of a low-temperature ferromagnetic (FM) state, as evidenced by the magnetization curves measured under applied magnetic fields of 5 mT and 5 T in Fig. 3(a). Furthermore, the gradual decrease of the low-field $M(T)$ curves, together with the broad minimum observed in the derivative curve dM/dT *versus* T (shown in Fig. S1 in the SI), suggests the absence of a single, well-defined value of the Curie temperature (T_C). Instead, a distribution of T_C values (around 125–160 K) provides a more accurate description. This can be attributed to variations in magnetic behaviour between the nanocrystals and the disordered intergranular or grain boundary regions in the ribbons, despite overall compositional homogeneity. The latter is an effect previously reported in other R-based nanocrystalline ribbons.[27,29]

Additionally, the splitting between the low-field $M_{ZFC}(T)$ and $M_{FC}(T)$ curves [see Fig. 3(a)] resembles a broadened Hopkinson peak. Such a peak typically appears just below T_C in ferromagnetic materials exhibiting structural disorder and surface effects. These factors enhance the peak's prominence because thermally activated unblocking of magnetic moments outweighs the intrinsic loss of magnetization as temperature increases.

In our case, the ZFC curve measured at 5 mT displays a more defined peak, consistent with the columnar-like microstructure observed *via* SEM. In contrast, the FC curve shows a more gradual, "catenary"-like decline with decreasing temperature. When normalizing both ZFC and FC curves to the maximum magnetization value near T_C, the relative values of the magnetization at 2 K are approximately 0.4 and 0.92, respectively. Similar behaviour has been reported in other melt-spun or nanostructured magnetocaloric alloys, such as Gd_5Si_4-type structure, HoB_2 and R_2Fe_{17} (R = Pr, Nd).[27,32,33] These studies support our interpretation that the enhanced definition of the ZFC peak is consistent with the microstructural characteristics of the ribbon samples. This indicates that the FC curve tails off more gradually when the temperature is lowered upon cooling, because the magnetic moments are easily aligned under the magnetic field on cooling from the paramagnetic phase. Due to the broad distribution of microstructural features, neither the ZFC nor the FC curves allow a precise determination of the Curie temperature.

In contrast, the $M(T)$ curve measured under a high field of 5 T exhibits a behaviour characteristic of a ferromagnet approaching saturation at low temperatures. In fact, at 2 K the magnetization exceeds 150 Am^2 kg^{-1} ($\sim 6.6\mu_B$ f.u.$^{-1}$ or μ_B per Gd, because we assume that only Gd is magnetic in GdFeSi alloy), as shown in Fig. 3(a). This value agrees well with that reported by Welter *et al.*[16] and is slightly higher than those found in bulk alloys produced *via* conventional melting followed by prolonged (2–5 weeks) high-temperature annealing at 1173 K, which yield values ranging from 120 to 130 Am^2 kg^{-1}.[18,34,35] However, the estimated Gd magnetic moment remains below the expected $7.0\mu_B$ per Gd^{3+} ion. This shortfall is likely due to structural and magnetic disorder at the grain boundaries

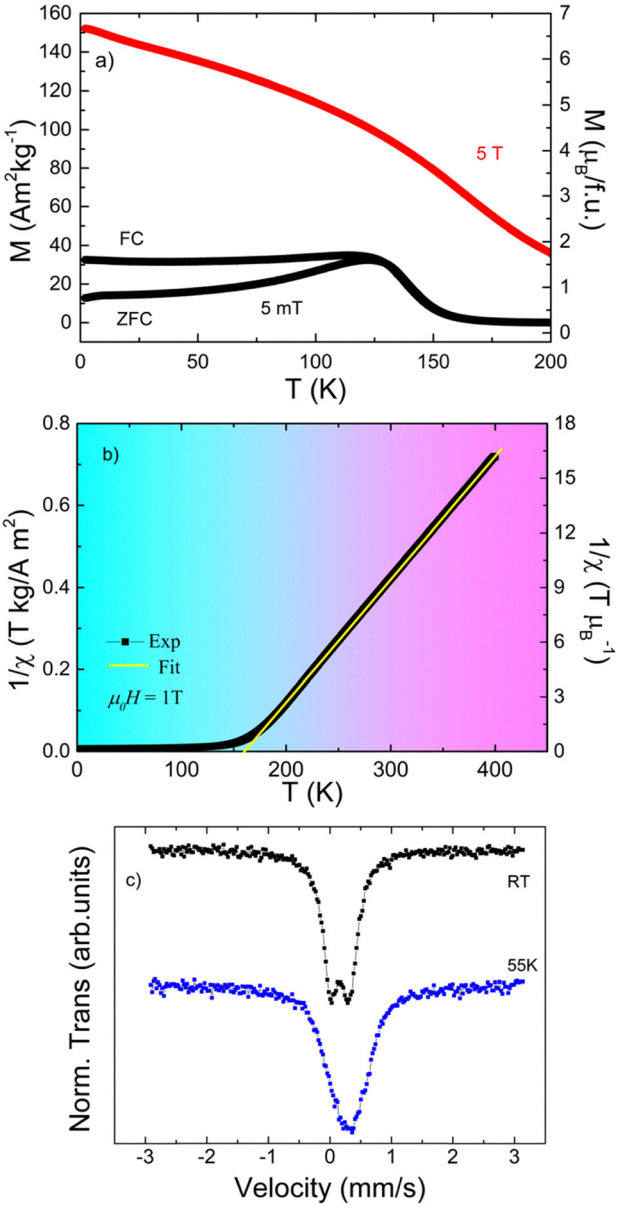

Fig. 3 (a) Magnetization dependence of temperature on ZFC-FC protocol under 5 mT and FH for 5 T applied magnetic field, (b) temperature dependence of the inverse magnetic susceptibility together with the Curie–Weiss law fit under 1 T applied magnetic field and (c) Mössbauer spectra measured at RT and 55 K. Details about the units are provided in Note S2 of the si.

between columnar-like regions. More plausibly, the anisotropic nature of the classical dipole interaction, specifically the demagnetizing field, gives rise to small magnetic domains with moments oriented at angles deviating from the applied magnetic field. This effect would depend on both the sample's shape and the strength of the applied magnetic field.

The temperature dependence of the inverse magnetic susceptibility, χ^{-1}, under an applied magnetic field of $1 - T$ together with the fit to a Curie–Weiss law for $T > T_C$ is shown in Fig. 3(b). The fit yields a paramagnetic Curie temperature of θ_P = 156.8 (2) K and an effective paramagnetic moment μ_{eff} = 8.078 (1)μ_B, which is close to the expected theoretical value for the Gd^{3+} free ion (7.94μ_B) and in good agreement with previously reported data.[16,34] No effective paramagnetic moment from Fe was needed for accounting for the slope of χ^{-1}. Further support for this "non-magnetic" Fe state comes from density-of-states calculations, which reveal hybridization between the p orbitals of Si and the d orbitals of Fe, likely responsible for the suppression of the Fe magnetic moment.[36] Additional evidence is provided by the absence of any magnetic sextet in the ^{57}Fe Mössbauer spectra [see Fig. 3(c)], indicating that the Fe atoms are not magnetically ordered well below T_C (see the spectrum measured at 55 K), which is consistent with the conclusions drawn from the Curie–Weiss law analysis. In any case, based on the measured value of the quadrupole splitting, it can be inferred that the hyperfine magnetic field does not exceed 1–3 T, a range typical for fields arising from dipolar interactions with the magnetic moments of neighbouring atoms.

Fig. 4(a) and (b) show the isothermal magnetization curves, $M(H)$, measured in the temperature interval between 90 and 190 K, along with the corresponding Arrott plots. It is worth noting that $M(H)$ curves do not reach full saturation even under a magnetic field of 5 T. The Arrott plots reveal a change in concavity from positive to negative, which according to Banerjee's criterion[37,38] indicates a second-order phase transition from ferromagnetic (FM) to paramagnetic (PM) behaviour at a

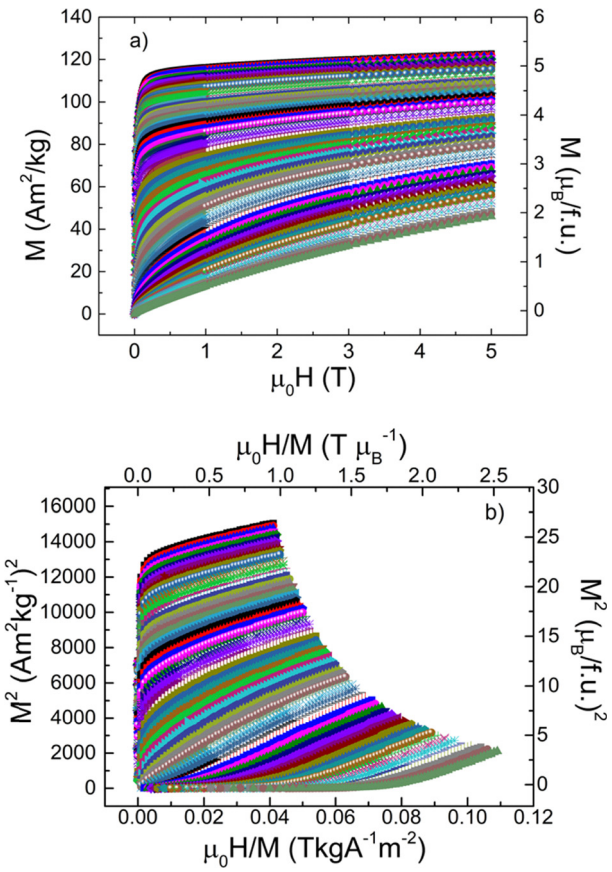

Fig. 4 (a) Magnetization isotherms and (b) Arrott plots of GdFeSi measured from 190 to 90 K with ΔT = 1.5 K.

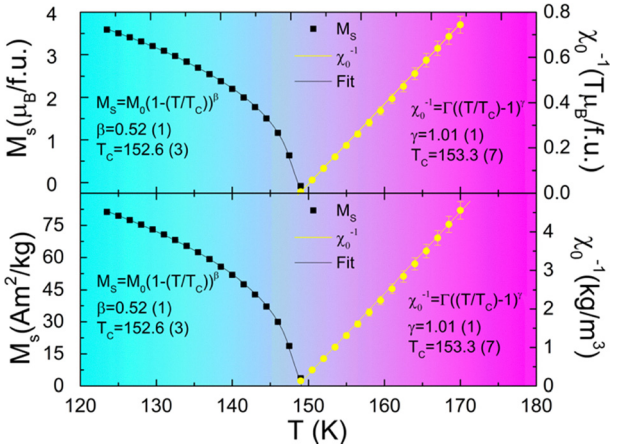

Fig. 5 Temperature dependences of the spontaneous magnetization and the inverse of the magnetic susceptibility together with the fits to the Kouvel–Fisher equations.

transition temperature T_C around 153 K, slightly above the value estimated from the minimum of the dM/dT *vs.* T curve (see Fig. S1 in the SI).

To explore in more detail the magnetic behaviour of GdFeSi in the immediacy of the FM–PM transition, we calculated the critical exponents β, γ, and δ from Arrott plots using the Kouvel–Fisher method.[38,39] Fig. 5 presents the temperature dependence of both the spontaneous magnetization and the inverse of the magnetic susceptibility together with the critical exponents obtained by fitting the Arrott plots to the universal scaling laws. The critical exponents, β = 0.52(1), γ = 1.01(1), and δ = 2,94 (6), the latter derived using the Widom scaling relation, $\delta = 1 + \gamma/\beta$,[40] are very close to those expected for a mean-field (MF) model (0.5, 1 and 3, respectively).[38,41,42] Small deviations are attributed to finite-size effects, microstructural inhomogeneity, and experimental uncertainties inherent to melt-spun ribbons.

Magnetocaloric properties

The variation of the isothermal magnetic entropy change, $|\Delta S_M|$, as a function of temperature under different applied magnetic field changes is depicted in Fig. 6(a). $|\Delta S_m|$ was calculated from isothermal magnetization (M–H) measurements using the Maxwell relation (see Note 3 of the SI). The maximum value, $|\Delta S_M|^{max}$, increases from 2 J k^{-1} K^{-1} to 6.7 J kg^{-1} K under magnetic field changes from 1 to 5 T, respectively. Although the MF critical analysis provides a good description of the isothermal $M(H)$ curves, surprisingly, the shape of the $|\Delta S_M|(T)$ curve is symmetric with respect to the temperature corresponding to the $|\Delta S_M|^{max}$ value.

This behaviour contrasts with the caret-like shape commonly observed in most materials exhibiting a magnetocaloric effect near a second-order magnetic phase transition, as illustrated in Fig. 6(b). In this figure, the MF prediction is compared with experimental data using normalized variables. While the MF model (details regarding the mean-field approximation calculation are provided in Note S4 of the SI) accurately describes the magnetically ordered phase, noticeable deviations occur in the paramagnetic region, which may be attributed to spin fluctuations

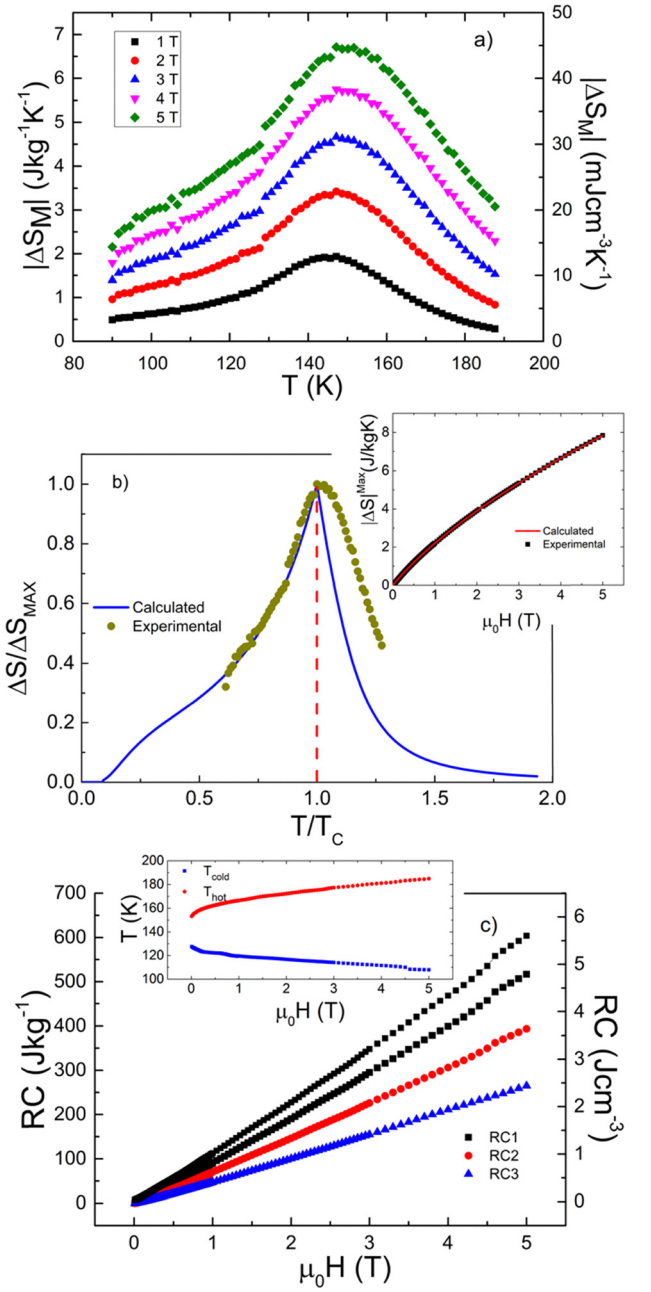

Fig. 6 (a) Isothermal magnetic entropy change as a function of temperature under different applied magnetic field changes, (b) comparation between calculated and experimental normalized magnetic entropy change under a 5 T applied magnetic field change (inset: calculated and experimental $|\Delta S_M|^{max}$ dependence with the applied magnetic field at $T = T_C$); and (c) RC dependence on the applied magnetic field change (inset: evolution of the temperatures corresponding to the hot and cold reservoirs). Details about the units are provided in Note S2 of the SI.

or magnetic short-range correlations. This symmetric and broadened profile of $|\Delta S_M|$ is particularly attractive for its potential use as a low-temperature magnetic refrigerant. The $|\Delta S_M|(T)$ curve is wide, providing an expanded temperature range of around $\Delta T \approx$ 20 K that can be considered as a "table-like" region,[43] which in turn optimizes a hypothetical Ericsson refrigeration cycle.

Moreover, the temperature corresponding to $|\Delta S_M|^{max}$ shifts to higher values as the applied magnetic field change increases, similar to that behaviour observed in certain R-based amorphous alloys.[44,45] Based on Landau's theory of second-order magnetic phase transitions within the MF approximation, the field dependence of $|\Delta S_M|^{max}$ can be described as:[46,47]

$$|\Delta S_M|^{max} = A(H + H_0)^{2/3} - AH_0{}^{2/3} + BH^{4/3} \quad (1)$$

where A and B are intrinsic parameters related to the GdFeSi material, while H_0 is an extrinsic parameter primarily determined by the purity and microstructure of the samples. The growth of $|\Delta S_M|^{max}$ should slow down as an indication of approaching saturation. In our case, the values obtained from the refinement of the experimental data to eqn (1) shown in Fig. 6(b) are: $A\mu_0{}^{-2/3}$ = 3.506(16) J/(kg K $T^{2/3}$)$^{-1}$, $B\mu_0{}^{-4/3}$ = −0.063(2) J/(kg K $T^{4/3}$)$^{-1}$, and $\mu_0 H_0$ = 0.081(4) T.

The H_0 parameter, which is proportional to the distribution of transition temperatures,[48,49] is significantly large, indicating a broad distribution of ordering temperatures and strain effects in the ribbon sample, leading to a broader $\Delta S_M(T)$ curve. This is further corroborated by the increase in the full width at half maximum ($\delta T_{FWHM} = T_{hot} - T_{cold}$) (see Table 1). The values obtained from the fit align with those reported in the literature concerning other magnetic systems undergoing second-order magnetic phase transitions, such as the 2 : 17 alloy $Pr_{1.64}Sm_{0.36}Fe_{17}$ or other families of compounds, including $Mn_5Ge_{3-x}Zn_x$, $Gd_{1-x}Sm_xCo_2$, and Ni-doped MnCoGe.[50–52] Table 1 summarizes a comparison of the MCE properties of GdFeSi for both bulk[33] and ribbon samples. It is worth noting the improvement of *circa* 20% in the value of $|\Delta S_M|^{max}$ for the ribbon sample.

Several attempts have been considered to estimate the so-called refrigerant capacity or relative cooling power (RC), a measure of how much heat can be transferred from the cold end to the hot end of a refrigerator during a thermodynamic cycle. One common method involves not only considering the maximum value shown in Fig. 6(a) but also the width of the $|\Delta S_M|(T)$ curve. RC values estimated using three different methods[49] are also shown in Fig. 6(c) and summarized in Table 1. The field dependencies of the calculated RC are nearly linear for the three refrigerant capacities (RC-1, RC-2 and RC-3).[48] For the GdFeSi ribbons, the calculated values under $\mu_0\Delta H$ = 5T are RC-1 = 517 J kg^{-1}, RC-2 = 394 J kg^{-1} and RC-3 = 265 J kg^{-1}. Notably, these values are up to 40% higher for the ribbon sample (see Table 1).

This enhancement has also been reported in other nanostructure materials as well, especially when an appropriate balance is maintained between the magnitude of $|\Delta S_M|$ and its FWHM.[43] To highlight the effect of microstructural refinement, we compare the melt-spun GdFeSi ribbons with previously reported bulk samples. Although the bulk data are from the literature, the measurements were performed under comparable magnetic fields and temperature ranges. The ribbons exhibit a sharper ZFC peak and a broader $|\Delta S_M|$ profile, reflecting the influence of the fine-grained microstructure on magnetic ordering and magnetocaloric performance. In the SI (Table S1), the current $|\Delta S_M|$ and RC values of GdFeSi are compared with those of other magnetocaloric materials of interest for low-temperature magnetic refrigeration in the 100–200 K range. Although the $|\Delta S_M|$ magnitude of the GdFeSi ribbon is of intermediate value, its RC is notably higher than that of most other intermetallic compounds, except for those with a higher rare-earth content, such as Dy_5Si_4 and $Gd_{55}Al_{25}Co_{20}$. The values obtained for DyFeSi are particularly competitive for potential use in magnetic refrigeration. From a fabrication and scalability perspective, ribbon production methods are more easily adaptable to practical cooling devices. However, in some cases, ribbons exhibit significantly reduced adiabatic temperature changes compared to their bulk counterparts, highlighting the need for further comprehensive investigation. Specifically, the tetragonal crystal structure of GdFeSi provides a framework for strong ferromagnetic coupling between Gd moments mediated by Fe, which determines the Curie temperature (~150 K). The melt-spun ribbons exhibit fine, homogeneous grains (~25 nm), reducing structural defects and magnetic inhomogeneity. This structural refinement enhances magnetic ordering, sharpens the ZFC peak, and influences the shape and width of the magnetocaloric RC profile. The combination of the atomic-level crystal structure and the nano-scale microstructure thus governs both the magnitude and temperature dependence of the magnetization and magnetocaloric response. The Curie temperature of the GdFeSi ribbons falls within the intermediate-temperature range of 100–200 K, relevant for applications in liquefaction of industrial gases such as nitric oxide (121.4 K), krypton (119.8 K), and nitrous oxide (184.7 K). Furthermore, the broad ΔS_m profile observed over this temperature range enhances the material's practical utility, demonstrating the potential of GdFeSi ribbons as intermediate-temperature magnetocaloric materials where few alternatives currently exist.

Table 1 Curie temperature, maximum isothermal magnetic entropy change $|\Delta S_M|^{max}$ and refrigerant capacity RC-1 for GdFeSi ribbon and bulk samples

Sample	T_C (K)	$\mu_0\Delta H$ (T)	$\lvert\Delta S_M\rvert^{max}$ (J kg^{-1} K)	RC-1 (J kg^{-1})	Ref.
Ribbons	150	5	6.7	517	This work
Bulk	135	5	5.4	373	34

Summary and concluding remarks

The magnetic and magnetocaloric properties of the GdFeSi alloy produced by melt-spinning were thoroughly investigated. The alloy crystallizes in a tetragonal crystal structure (space group *P*4/*nmm*) and exhibits an average grain size of 25(3) nm. Magnetization measurements confirm that the alloy is ferromagnetic with a Curie temperature value around 150 K. This ferromagnetic order seems to be due to Gd ions exclusively, because Mössbauer spectrometry clearly shows the absence of any sextet coming from the hypothetical magnetic ordering of the Fe ions. The critical exponents obtained from modified Arrott plots (β = 0.52, γ = 1.01, and δ = 2.94) are consistent with mean-field theory, indicating the presence of long-range magnetic interactions.

However, due to the nanostructured nature of GdFeSi, the existence of magnetic disorder, particularly at the grain boundaries, cannot be ruled out. Notably, some deviation is observed in the normalized isothermal magnetic entropy change *versus* temperature for $T > T_C$ between the experimental and mean-field-calculated curves. This discrepancy is likely attributed to localized disordered phases, spin fluctuations, or short-range magnetic correlations. A key finding is the broadening of the isothermal magnetic entropy change curve, which leads to an extended temperature range with a significant entropy change. This broadening markedly enhances the refrigerant capacity of GdFeSi compared to its bulk counterpart. Overall, these results underscore the potential of GdFeSi ribbons as promising materials for magnetocaloric applications.

Author contributions

A. S.-P. & J. L. S. L. conceptualization, investigation, data curation, methodology and formal analysis, writing original draft; J. L.-G. & L. E. data curation, and formal analysis; J. L.-G. data analysis, validation; J. A. B. investigation, data curation; P. G. & P. A.-A. conceptualization, supervision, funding acquisition. All the authors participated in the writing of the final version.

Conflicts of interest

There are no conflicts to declare.

Data availability

The data supporting this article have been included in the paper.

Supplementary information (SI) is available, including details about the determination of the Curie temperature and isothermal magnetic entropy, the conversion of magnetic and magnetocaloric units, the mean-field approximation calculation, and a table with magnetocaloric parameters of some relevant alloys for comparison. See DOI: https://doi.org/10.1039/d5tc02968f.

Acknowledgements

This work has been partially supported by the following projects: (a) PTDC/EMETED/3099/2020, UIDP/04968/2020-Programático; (b) PID2022-138256NB-C21, from Spanish MCIN/AEI/10.13039/501100011033 and ERDF, UE; GRU-GIC-24-113, from SEKUENS, Principality of Asturias, Spain, and; (c) CF-2023-I-2143 from CONAHCYT and Laboratorio Nacional de Nanociencias y Nanotecnología (LINAN IPICyT), Mexico. Authors would like to acknowledge the technical support provided by MSc B. A. Rivera, MSc A. I. Peña Maldonado and Dr. I. Becerril Juarez (LINAN technical staff) and by Servicios Científico-Técnicos de la Universidad de Oviedo. L. G. Escobedo-Valadez thanks SECIHTI for supporting his PhD studies at IPICyT (fellowship No. 4024938).

Notes and references

1 K. A. Gschneidner and V. K. Pecharsky, *Int. J. Refrig.*, 2008, **31**, 945.
2 V. Franco, J. S. Blázquez, J. J. Ipus, J. Y. Law, L. M. Moreno-Ramírez and A. Conde, *Prog. Mater. Sci.*, 2018, **93**, 112.
3 M. S. Reis, *Coord. Chem. Rev.*, 2020, **417**, 213357.
4 Y. Wang, H. Pan and S. Liu, *J. Supercond. Nov. Magn.*, 2025, **38**, 86.
5 S. Mellari, *Int. J. Air-Cond. Refrig.*, 2023, **31**, 5.
6 N. T. M. Duc, H. Srikanth and M.-H. Phan, *Sci. Technol. Adv. Mater.*, 2025, **26**, 2546287.
7 W. Liu, T. Gottschall, F. Scheibel, E. Bykov, A. Aubert, N. Fortunato, B. Beckmann, A. M. Döring, H. Zhang, K. Skokov and O. Gutfleisch, *J. Alloys Compd.*, 2024, **995**, 174612.
8 G. Green, W. Patton and J. Stevens, in *Advances in Cryogenic Engineering*, ed. R. W. Fast, Springer, US, Boston, MA, 1988, p. 777.
9 M. Guel-Rodríguez, J. Zamora, C. F. Sánchez-Valdés, J. L. S. Llamazares and P. Álvarez-Alonso, *J. Alloys Compd.*, 2024, **978**, 173452.
10 J. Li, S. Ma, H. Wang, W. Gong, J. Jiang, S. Li, Y. Wang, D. Geng and Z. Zhang, *J. Mater. Sci. Technol.*, 2014, **30**, 973.
11 L. Li and M. Yan, *J. Alloys Compd.*, 2020, **823**, 153810.
12 Y. Zhang, *J. Alloys Compd.*, 2019, **787**, 1173.
13 H. Zhang, Y. J. Sun, E. Niu, L. H. Yang, J. Shen, F. X. Hu, J. R. Sun and B. G. Shen, *Appl. Phys. Lett.*, 2013, **103**, 202412.
14 H. Zhang, R. Gimaev, B. Kovalev, K. Kamilov, V. Zverev and A. Tishin, *Phys. B*, 2019, **558**, 65.
15 O. I. Bodak, E. I. Gladyshevskii and P. I. Kripyakevich, *J. Struct. Chem.*, 1970, **11**, 283.
16 R. Welter, G. Venturini and B. Malaman, *J. Alloys Compd.*, 1992, **189**, 49.
17 N. Zaidi and A. Cherif, *AIP Adv.*, 2023, **13**, 045118.
18 H. Zhang and B.-G. Shen, *Chin. Phys. B*, 2015, **24**, 127504.
19 H. Zhang, Y. J. Sun, L. H. Yang, E. Niu, H. S. Wang, F. X. Hu, J. R. Sun and B. G. Shen, *J. Appl. Phys.*, 2014, **115**, 063901.
20 S. Talakesh and Z. Nourbakhsh, *J. Supercond. Nov. Magn.*, 2017, **30**, 2143.
21 S. Talakesh and Z. Nourbakhsh, *Indian J. Phys.*, 2019, **93**, 571.
22 X. B. Liu and Z. Altounian, *J. Appl. Phys.*, 2010, **107**, 09E103.
23 H. Zhang, B. G. Shen, Z. Y. Xu, J. Shen, F. X. Hu, J. R. Sun and Y. Long, *Appl. Phys. Lett.*, 2013, **102**, 092401.
24 J. L. Sánchez Llamazares, P. Ibarra-Gaytán, C. F. Sánchez-Valdés, P. Álvarez-Alonso and R. Varga, *J. Alloys Compd.*, 2019, **774**, 700.
25 P. J. Ibarra-Gaytan, C. F. Sánchez-Valdes, J. L. Sánchez Llamazares, P. Álvarez-Alonso, P. Gorria and J. A. Blanco, *Appl. Phys. Lett.*, 2013, **103**, 152401.
26 J. L. Sánchez Llamazares, C. F. Sánchez-Valdes, P. J. Ibarra-Gaytan, P. Álvarez-Alonso, P. Gorria and J. A. Blanco, *J. Appl. Phys.*, 2013, **113**, 17A912.
27 J. L. G. Álvarez, P. Álvarez-Alonso, C. F. Sánchez-Valdés, J. A. Blanco, P. Gorria and J. L. Sánchez Llamazares, *J. Alloys Compd.*, 2024, **979**, 173575.

28 J. L. Sánchez Llamazares, P. Álvarez-Alonso, C. F. Sánchez-Valdés, P. J. Ibarra-Gaytán, J. A. Blanco and P. Gorria, *Curr. Appl. Phys.*, 2016, **16**, 963.
29 C. F. Sánchez-Valdés, P. J. Ibarra-Gaytán, J. L. Sánchez Llamazares, M. Ávalos-Borja, P. Álvarez-Alonso, P. Gorria and J. A. Blanco, *Appl. Phys. Lett.*, 2014, **104**, 212401.
30 J. Rodríguez-Carvajal, *Phys. B*, 1993, **192**, 55.
31 D. Martínez-Blanco, P. Gorria, J. A. Blanco, M. J. Pérez and J. Campo, *J. Phys.: Condens. Matter*, 2008, **20**, 335213.
32 J. H. Belo, A. M. Pereira, C. Magen, L. Morellón, M. R. Ibarra, P. A. Algarabel and J. P. Araujo, *J. Appl. Phys.*, 2013, **112**, 133909.
33 L. G. Escobedo-Valadez, K. Padrón-Alemán and J. L. Sánchez Llamazares, *J. Alloys Compd.*, 2025, **1039**, 183235.
34 M. Napoletano, F. Canepa, P. Manfrinetti and F. Merlo, *J. Mater. Chem.*, 2000, **10**, 1663.
35 A. G. Kuchin, S. P. Platonov, V. S. Gaviko and M. Y. Yakovleva, *J. Phys.: Conf. Ser.*, 2019, **1389**, 012128.
36 S. Gupta and K. G. Suresh, *J. Alloys Compd.*, 2015, **618**, 562.
37 D. C. Jiles, *Introduction to Magnetism and Magnetic Materials*, CRC Press (1998).
38 N. G. Bebenin, R. I. Zainullina, V. V. Ustinov and Y. M. Mukovskii, *J. Magn. Magn. Mater.*, 2014, **354**, 76.
39 H. Liu, J. Fan, D. Hu, J. L. Sanchez Llamazares, P. Gorria, C. Ma, Y. Zhu and H. Yang, *Mater. Res. Bull.*, 2023, **164**, 112239.
40 B. Widom, *J. Chem. Phys.*, 1964, **41**, 1633.
41 R. Cabassi, F. Bolzoni, A. Gauzzi and F. Licci, *Phys. Rev. B: Condens. Matter Mater. Phys.*, 2006, **74**, 184425.
42 K. Murugan, P. Govindaraj, S. Paulraj and K. Venugopal, *Mater. Res. Bull.*, 2024, **179**, 112966.
43 P. Alvarez, p Gorria, J. L. Sanchez Llamazares and J. A. Blanco, *J. Alloys Compd.*, 2013, **568**, 98.
44 L. Xue, L. Shao, Q. Luo and B. Shen, *J. Alloys Compd.*, 2019, **790**, 633.
45 Y. Zhang, J. Zhu, S. Li, B. Zhang, Y. Wang, J. Wang and Z. Ren, *J. Alloys Compd.*, 2022, **895**, 162633.
46 J. Lyubina, *et al.*, *Phys. Rev. B: Condens. Matter Mater. Phys.*, 2011, **83**, 012403.
47 P. Alonso, P. Gorria and J. A. Blanco, *Phys. Rev. B:Condens. Matter Mater. Phys.*, 2011, **84**, 024412.
48 P. Gorria, J. L. Sánchez Llamazares, P. Alvarez, M. J. Perez, J. Sanchez Marcos and J. A. Blanco, *J. Phys. D: Appl. Phys.*, 2008, **41**, 192003.
49 H. Jaballah, *et al.*, *J. Phys. Chem. Solids*, 2022, **161**, 110438.
50 H. Jin, *et al.*, *Phys. Lett. A*, 2023, **474**, 128819.
51 S. Bellafkih, H. Jaballah and L. Bessais, *Phys. Chem. Solids*, 2023, **178**, 111355.
52 S. Sakthivel, *et al.*, *Appl. Phys. A: Mater. Sci. Process.*, 2023, **129**, 428.

